Pauli Exclusion Pricniple Violation Analysis with NEMO3 and Calorimeter R&D for SuperNEMO

Anastasia Freshville

Supervisor:
Dr Ruben Saakyan

June 2, 2008

Abstract

The primary target of the NEMO3 detector is to search for $0\nu\beta\beta$ decay and study $2\nu\beta\beta$ decay in greater depth. However, the data collected with the experiment provides an opportunity to search for non-Paulian transitions of ^{12}C found in the scintillators of the detector. This report presents the analysis and the limit obtained: $T_{1/2} > 8.9 \times 10^{25}$ years at 90% CL.

The proposed SuperNEMO experiment, a next generation $0\nu\beta\beta$ experiment, is currently in its R&D phase. One of the most important requirements for SuperNEMO is to have an extremely good energy resolution therefore the calorimeter design is of utmost importance. The report considers and presents findings of using an alternative calorimeter design based on scintillator bars.

Acknowledgements

I would like to thank Ruben Saakyan for helping me to finally settle into my PhD and for providing constant help and guidance. Thank you to the UCL HEP and NEMO groups for helping me get stuck in. And a final thank you to Mark Lancaster for getting me started.

Contents

List of Figures

List of Tables

1 Introduction

In early nuclear beta decay experiments it was thought that a nucleus A transformed into a lighter nucleus B accompanied by an electron emission ($A \longrightarrow B + e^-$). However, the electron was observed to have a spectrum of energies rather than an expected fixed energy. To explain this phenomenon, in 1930 Wolfgang Pauli proposed the neutrino - an electrically neutral particle emitted alongside the electron that carries off the the "missing" energy. In the mid-fifties Cowan and Reines detected the neutrino at the Savannah River nuclear reactor whilst studying inverse beta decay, confirming the theory. The muon and tau neutrino discoveries were followed in 1963 and 2000 respectively. [1]

As neutrinos are always found to be emitted with left helicity the Standard Model assumes the particle to be massless. In 1957, Bruno Pontecorvo suggested that if neutrinos had non-zero mass then they could oscillate between a neutrino and antineutrino (by analogy with the Kaon sector) [2]. This idea was later developed into neutrino oscillations between flavour eigenstates. Experiments such as Super-Kamiokande and SNO have shown that this is correct - the neutrino undergoes flavour changes during oscillations via mixing between neutrino mass and weak interaction eigenstates. An example of this can be seen in Equation 1, showing a two neutrino approximation oscillation framework for $\nu_\mu \longrightarrow \nu_\tau$ oscillations [3].

$$\begin{pmatrix} \nu_\mu \\ \nu_\tau \end{pmatrix} = \begin{pmatrix} \cos\theta & -\sin\theta \\ \sin\theta & \cos\theta \end{pmatrix} \begin{pmatrix} \nu_1 \\ \nu_2 \end{pmatrix} \tag{1}$$

This implies that at least one of the neutrinos must have a non-zero mass, contradicting the Standard Model. The mass difference between neutrino mass eigenstates 2 and 3 (the larger of the two mass splittings) obtained from the Super-Kamiokande experiment is shown in Equation 2 [4].

$$\Delta m^2_{23} = \Delta m^2_{atmospheric} = 2.5 \times 10^{-3}\ \text{eV}^2 \tag{2}$$

Whilst neutrino oscillations have given us great insight into the neutrino there are some questions they cannot answer. Oscillations give us the mass difference between eigenstates, however not the absolute mass of the neutrino. Even if one of the neutrinos in this mass splitting has no mass, taking $\sqrt{\Delta m^2_{23}}$ from Equation 2 gives an electron neutrino mass of 0.05 eV.

As neutrinos are neutral particles the theory of weak interaction presents the possibility that the neutrino could be its own antiparticle, as proposed by Ettore Majorana, known as a 'Majorana' particle [5]. Neutrino oscillations cannot shed any light on the nature of the neutrino. One of the best tools to answer the two questions posed is neutrinoless double beta decay ($0\nu\beta\beta$).

2 Double Beta Decay

Double beta decay ($2\nu\beta\beta$) is a process which occurs when simple beta decay is not energetically favourable. In this process two neutrons simultaneously transform into two protons, emitting two electrons and two antineutrinos, as in Equation 3.

$$2n \longrightarrow 2p + 2e^- + 2\overline{\nu}_e \tag{3}$$

If neutrinos are Majorana particles, a possibility for $0\nu\beta\beta$ occurs, violating lepton number conservation (Equation 4). This process is shown in Figure 1.

$$2n \longrightarrow 2p + 2e^- \tag{4}$$

In order to gain further insight into the process it can be seen to occur in two stages:

$$1)\ n \longrightarrow p + e^- + \text{`}\overline{\nu}\text{'} \tag{5}$$

In Equation 5 we see that in order for the lepton number to be conserved the neutrino must be emitted with right helicity (as an antineutrino).

$$2)\ \text{`}\nu\text{'} + n \longrightarrow p + e^- \tag{6}$$

The neutrino in Equation 6 must flip helicity to left helicity in order to conserve angular momentum at this stage of the process. This can be done by selecting a reference frame that is moving faster than the neutrino, requiring the Majorana neutrino to have mass.

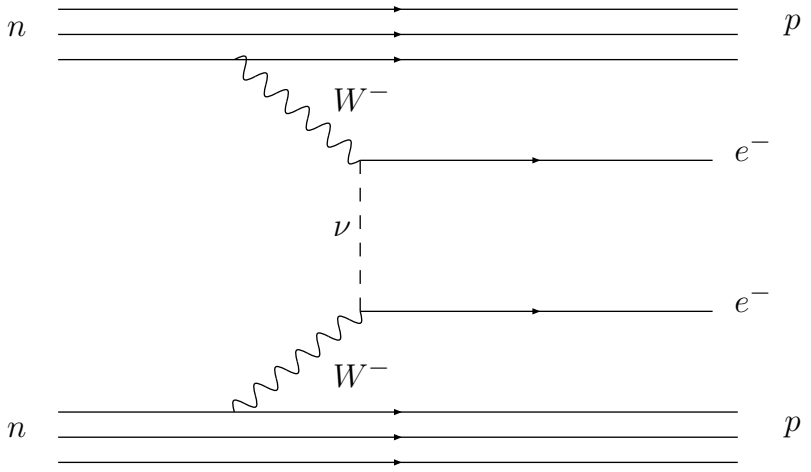

Figure 1: Neutrinoless double beta decay

The halflife measured from $0\nu\beta\beta$ experiments can be directly related to the electron neutrino mass:

$$[T^{0\nu}_{1/2}]^{-1} = G^{0\nu}|M^{0\nu}|^2\langle m_{\nu_e}\rangle^2 \tag{7}$$

where $[T^{0\nu}_{1/2}]$ is the measured halflife, $G^{0\nu}$ is the phase space (proportional to the Q value of the $0\nu\beta\beta$ isotope (the energy available for the decay): $G^{0\nu} = (Q_{\beta\beta})^5$), $|M^{0\nu}|$ is the nuclear matrix element and $\langle m_{\nu_e}\rangle$ is the effective neutrino mass.

In comparison, $2\nu\beta\beta$ decay cannot give us any information on the neutrino mass:

$$[T^{2\nu}_{1/2}]^{-1} = G^{2\nu}|M^{2\nu}|^2 \tag{8}$$

Although the nuclear matrix elements $|M^{0\nu}|$ and $|M^{2\nu}|$ are different for $0\nu\beta\beta$ and $2\nu\beta\beta$ they are calculated in similar ways. A better understanding of $|M^{2\nu}|$ will help to constrain $|M^{0\nu}|$ and therefore get a more accurate result for neutrino mass from $0\nu\beta\beta$ decay. The study of $2\nu\beta\beta$ is also important as it comprises part of the background affecting the search for $0\nu\beta\beta$ decay (see Section 3.3) and therefore needs to be well understood.

The current best estimate of neutrino mass is by the Heidelberg-Moscow experiment [6]:

$$\langle m_{\nu e}\rangle < 0.3eV - 0.8eV \tag{9}$$

3 The NEMO3 Detector

The main goals of the NEMO3 detector (shown in Figure 2) are to study $0\nu\beta\beta$ decay to a halflife limit of 2×10^{24} years, corresponding to a sensitivity of $0.3 - 0.9$ eV for the effective neutrino mass and to carry out in depth studies of $2\nu\beta\beta$ (for nuclear matrix element calculations and background understanding). NEMO3 consists of 10 kg of source foils, containing seven isotopes for the study of double beta decay (^{100}Mo, ^{82}Se, ^{116}Cd, ^{130}Te, ^{150}Nd, ^{96}Zr and ^{48}Ca, with Q_β values ranging between 2.5 and 4.3 MeV) and two for background measurements (Cu and ^{nat}Te). The detector combines the techniques of a tracking wire chamber for particle identification with a calorimeter for energy and time measurements of the particles. The geometry of the detector is cylindrical with a height of 3 metres and a diameter of 5 metres (excluding the passive shielding of the detector). It is split into 20 equal sectors (Figure 2, right), each containing seven strips of source foils. It is situated in the Fréjus Underground Laboratory in Modane in France 1700 metres (4850 metres water equivalent) underground to shield the detector from cosmic ray background.

3.1 Tracker

The NEMO3 wire chamber provides three dimensional tracking of charged particles. There are nine layers of Geiger drift cells on either side of the source foils, positioned vertically in the volume. Each sector contains a total of 309 cells. The cells closest to the foils are important for vertex resolution of events, ensuring they originated in the source foils. A vertical magnetic field of 25 Gauss surrounding the detector and the tracking

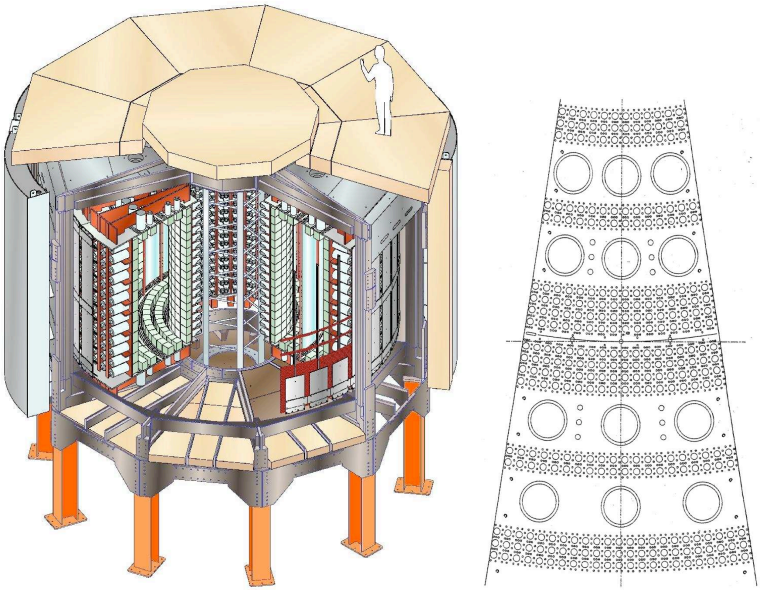

Figure 2: The NEMO3 detector (left) and sector (right)

volume provides rejection of electron-positron events (produced by a high energy photon interacting within the detector).

3.2 Calorimeter

The NEMO3 calorimeter provides energy measurements of the particles deposited and time of flight information used to reject external background events (electrons crossing through the detector). It consists of 1940 blocks of polystyrene scintillator containing the p-Terphenyl (PTP) scintillating agent and wavelength shifting POPOP. The blocks are coupled to low radioactivity 3 or 5 inch photomultiplier tubes (PMTs), depending on their position within the detector, through a plastic light guide. The scintillator blocks are wrapped in aluminised mylar foil (reflectivity coefficient of 90%) which helps to reflect light from the scintillators back to the PMTs increasing the efficiency of light collection. The scintillators are placed around the tracking volume (internal and extrenal walls) and at the top and bottom of the tracking volume (top and bottom petals), with the composition of the scintillator varying slightly between the wall and petal scintillators. The energy resolution of the calorimeter was measured to be $\sim$ 14% $\Delta E/E$ full width half maximum (FWHM) at 1 MeV. The time resolution of the detectir is $\sim$ 250 ps at 1 MeV.

3.3 Background

It is essential to be able to discriminate between real data and background events in NEMO3. The backgrounds can be thought of in two categories - internal backgrounds, originating from radioactive contaminants inside the double beta decay source foils, and external backgrounds, originating outside of the source foils.

3.3.1 Internal Background

An irreducible background for NEMO3 is the overlap of the $2\nu\beta\beta$ decay tail onto the $0\nu\beta\beta$ decay peak, as shown in Figure 3. For this reason the $2\nu\beta\beta$ spectrum must be well measured and the energy resolution of the detector is critical. The thickness of the source foils was designed so that the loss of energy effects in the foils would not be greater than the intrinsic resolution of the calorimeter.

There are two isotopes from the ^{232}Th and ^{238}U natural radioactivity chains that are dangerous to $0\nu\beta\beta$ decay in the 3 MeV region. These isotopes are ^{208}Tl with a Q_β value of 4.992 MeV coming from ^{232}Th and ^{214}Bi with a Q_β value of 3.270 MeV coming from ^{238}U. Both of the isotopes decay via β emission and can mimic double beta events by three mechanisms: beta decay accompanied by an internal conversion, Möller scattering or Compton scattering. Although both of these isotopes have short lifetimes they can contribute to the background greatly as they are in constant supply from their parent atoms.

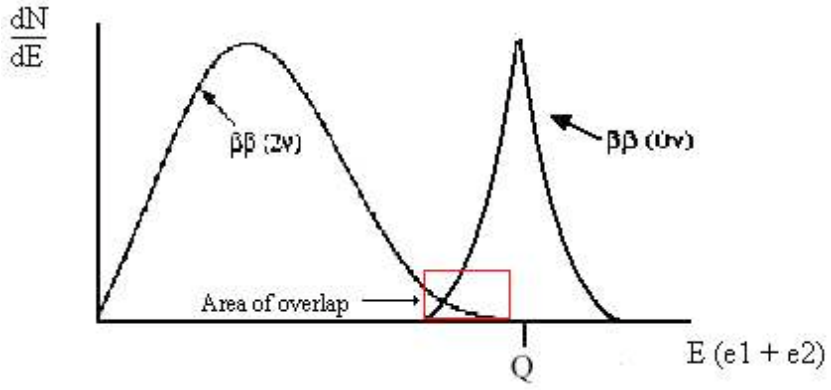

Figure 3: Overlap of $2\nu\beta\beta$ tail onto the $0\nu\beta\beta$ peak

3.3.2 External Background

An electron entering the detector at one point, interacting with the foil and exiting the detector is known as a crossing electron. This background is reduced by using time of flight information.

Other sources of external background in NEMO3 are photons interacting with the source foils. These photons can be produced by the natural radioactivity of the detector components (as described in Section 3.3.1), neutrons produced by spontaneous fission in the surrounding materials and detector components or by thermal neutron capture, photons coming from natural radioactivity in the surrounding rock and cosmic rays. The photons coming from the above sources can mimic an event in the following ways: pair creation (for $E_\gamma \geq 1.02$ MeV), Compton scattering followed by Möller scattering, double Compton scattering, photoelectric effect followed by Möller scattering and Compton scattering followed by the photoelectric effect. In order to reduce external backgrounds the detector is covered with a neutron shield comprising of paraffin, wood and water which thermalises fast moving neutrons so that they can then be stopped by the iron shield, which also attenuates γ rays.

A strong source of background comes from radon, which is a rare radioactive gas created by the decay of the ^{238}U chain. It can easily penetrate rock and the concrete coated walls of the laboratory into the air and diffuse into the detector, contaminating the experiment with ^{214}Bi, its daughter isotope, which can mimic double beta events. These events can be excluded using bismuth-polonium delay coincidence (using the daughter isotope of ^{214}Bi), however a large proportion still remains. NEMO3 has two phases of operations. Phase 1 data has high levels of radon (~ 15 Bqm^{-3}), while for Phase 2 of data taking an anti-radon factory was placed around the NEMO3 detector reducing the levels of radon significantly to 0.15 Bqm^{-3} by circulating air through a column of charcoal.

4 Pauli Exclusion Principle

The Pauli exclusion principle (PEP) states that no two identical fermions (which have half-integer spin) can occupy the same state simultaneously. This is a consequence of the wave function for two fermions being anti-symmetric. It is one of the most fundamental laws in nature without which everything would collapse down to a single point. Any direct violation of PEP found experimentally would have catastrophic implications for current theoretical models. It is very important to test the validity of PEP, which can be done experimentally by finding a halflife limit on its violation.

Experiments can search for PEP violation by looking for atoms or nuclei in a non-Paulian state or looking for evidence of transitions of atoms and nuclei into a non-Paulian state. The second approach can be used in NEMO3.

4.1 PEP and NEMO3

The plastic scintillators used in NEMO3 contain ^{12}C - a stable nucleus which has fully occupied shells. Using NEMO3 data a search can be carried out to look for transitions from the ^{12}C state to non-Paulian states. A halflife limit on PEP violation can then be extracted. There are two transitions to look for with ^{12}C.

The first is to look for the transition of a nucleon from the $1p_{3/2}$ shell to the fully occupied $1s_{1/2}$ shell (Figure 4a). This process is accompanied by γ-quantum emission, where the energy of the γ is equal to the

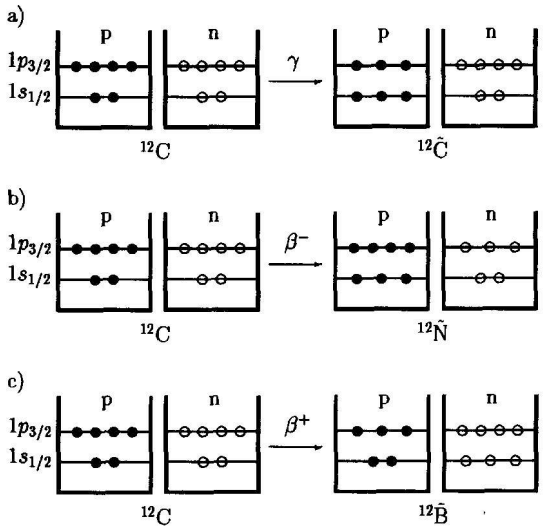

Figure 4: a) Transition of a proton from the p-shell to the fully occupied s-shell (a similar figure can be constructed for neutrons) b) non-Paulian β^- transition of ^{12}C to $^{12}\tilde{N}$ c) non-Paulian β^+ transition of ^{12}C to $^{12}\tilde{B}$ [7]

difference between the p and s energy levels ($\sim$ 20 MeV). The γ from the non-Paulian transition produced in the scintillator crosses the tracking volume, interacts with the source foil and undergoes pair production (the dominant process for $E_\gamma \sim 20$ MeV) to produce an electron-positron pair. This is seen as two tracks vertexing in the foil (which are coinciding events), each associated with a single scintillator hit.

The second is to look for a nucleon from the p shell falling to the fully occupied s shell via β decay (Figures 4b and c). This can happen via a β^- ($n \longrightarrow p + e^- + \overline{\nu}_e$) transition of ^{12}C for a neutron falling from the p shell to the fully occupied s shell. The emitted β^- are distributed as ordinary β^- decay spectra with a Q_β value of 20 MeV. A β^- emitted in the plastic scintillator crosses the tracking volume and the source foil and enters the opposite side of the detector. This can be seen as a crossing electron event identified by using time of flight information. This is seen as two tracks vertexing in the foil, each associated with a scintillator hit. This process can also happen via a β^+ ($p \longrightarrow n + e^+ + \nu_e$) transition of ^{12}C for a proton falling from the p shell to the fully occupied s shell. The efficiency for β^+ decay detection is lower as when interacting with matter a positron annihilates with an electron to create two photons with energies of 511 keV each.

4.2 γ Emission from Nucleon $\longrightarrow e^+e^-$ Analysis

4.2.1 Event Reconstruction

Both data and Monte Carlo (MC) events are reconstructed using the NEMOR package, which fits a track to the Geiger cell hits and reconstructs the event vertex, energy, timing information, etc. An example of a reconstructed data event can be seen in Figure 5, showing an electron-positron event with an energy of 7.7 MeV.

4.2.2 Event Selection

The 20 MeV γ produced in the scintillator from the non-Paulian transition crosses the tracking volume and interacts with the source foil, producing a coincident e^+e^- pair. In order to select an event of this kind we require two tracks originating in layers one to four of the detector (ensuring that the event is originating in the foil) of any curvature with the sum of the energies of the tracks $\geq$ 4 MeV. Each track must have a fired scintillator associated with it. The two reconstructed track intersections with the foil must be less than 4 cm apart in the x and y axis and less than 8 cm in the z axis. Although NEMO3's magnetic field allows the differentiation between electrons and positrons in the detector in this case this requirement is not used due to the high energies of the events looked at. At higher energies the magnetic field does not curve the particles as much as at lower energies (for double beta decay analysis), therefore making misidentification of particles more likely. In order to increase the acceptance of events particles of any curvature are looked for.

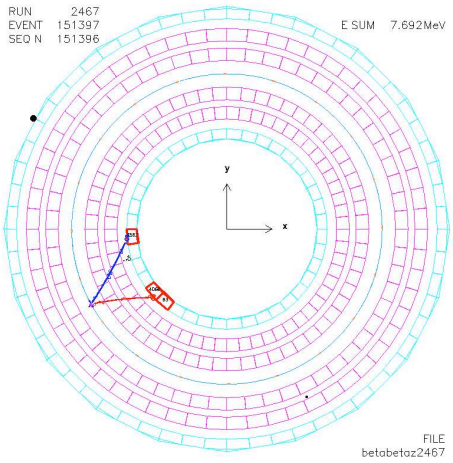

Figure 5: Reconstructed electron-positron event of 7.7 MeV energy

Badly reconstructed tracks and those produced by radon are removed. Non-associated fast hits (random hits in the wire chamber not associated to a track) and non-associated scintillator hits (random scintillator hits not associated to a track) are also removed.

Time of flight information is usually used in order to exclude crossing electron background and to select coincident tracks, as required for this analysis. However, at high energies the time of flight information is different for data and MC and is not well understood. High energy corrections for the probabilities of events being external or internal are required. Taking out this requirement lets a lot of crossing event background (such as the 20 MeV γ produced in the PEP violating transition interacting within the scintillator via Compton scattering, producing an electron which could cross the tracking volume) in, reducing the sensitivity. However, it is important to ensure that the selected events are well understood in order to make a correct efficiency calculation. A lot of further investigation needs to be made into this for the final analysis.

4.2.3 Monte Carlo Simulations

In order to produce MC simulations the NEMO3 detector was accurately described using GEANT3. $2\nu\beta\beta$, $0\nu\beta\beta$ and various backgrounds are simulated with the genBB package, which simulates the decay processes. GEANT then simulates the interactions possible within the detector, such as pair production, Compton scattering, etc. The MC simulation package is called NEMOS.

NEMOS only allows the simulation of scintillator walls and petals separately, therefore the analysis has to be divided into two parts. Ten million events were generated uniformly in the scintillator walls and petals separately for both Phase 1 and Phase 2 together. The selection cuts described in Section 4.2.2 were then applied to the data and the MC produced.

4.2.4 Calculating the Halflife Limit

Like other decays, Pauli-forbidden decays obey the radioactive decay equation:

$$N = N_0 e^{-\lambda t} \tag{10}$$

where N_0 is the number of initial atoms in the sample, N is the number of isotopes remaining in the sample after time t, $\lambda = \frac{ln2}{\tau_{1/2}}$ ($\tau_{1/2}$ = halflife) and t is the length of the measurement in years. As the halflives involved are very large (of the order of 10^{20} years or larger), λ is very small, making the exponential in Equation 10 extremely small meaning it can be Taylor expanded:

$$e^{-\lambda t} \approx 1 - \lambda t \tag{11}$$

Substituting Equation 11 into Equation 10 gives:

$$N_{decay} = N_0(1 - (1 - \lambda t)) = N_0 \lambda t \tag{12}$$

where $N_{decay} = N_0 - N$. Introducing the efficiency of the detector, η, into the equation:

$$N_{decay} = \eta N_0 \lambda t \tag{13}$$

where $N_0 = \frac{N_A m}{M}$, N_A is Avogadro's number $= 6.022 \times 10^{23}$ mol^{-1}, m is the isotope mass, g and M is the molar mass, gmol^{-1}.

The halflife limit at a 90% confidence level (CL) can then be obtained by rearranging Equation 13:

$$\tau_{1/2} > \frac{N_0}{N_{decay}^{90\%CL}} \eta ln2t \tag{14}$$

4.2.5 Results

The event selection was run on all of the available Phase 1 and Phase 2 approved reconstructed data. The same was done for the wall and petal MC simulations. The resulting events can be seen in Figure 6, which shows the sum of the energies of the two particles (a proton and electron combination). In the data distribution three peaks are seen between 4 and 5 MeV, at ~ 8 MeV and at ~ 22.5 MeV. The high energy peak at 22.5 MeV is attributed to the saturation of the PMTs (most likely by high energy muons). The PMTs used in NEMO3 get saturated by an energy of ~ 12 MeV, therefore for a sum of two high energy tracks saturation occurs at ~ 24 MeV, as seen in the data plot. The structure between 4 and 8.5 MeV is open to speculation. The peak between 4 and 5 MeV could be attributed to ^{208}Tl (which is part of the ^{232}Th decay chain) as it has a Q_β value of 4.992 MeV. Above 5 MeV there are two most likely sources of background: neutrons (and γs from neutron capture), which have a mostly flat distribution with a small peak at ~ 8 MeV (though this is not an overly prominent peak as shown by simulations) and extremely high energy muons. Muons, which are the minimum ionising particle, above 5 MeV would have a Landau distribution (a peak with a long tail, as seen in the data plot). However, only muons of extremely high energies would be able to penetrate the NEMO3 detector, implying that they would no longer act as minimum ionising particles as they have undergone bremsstrahlung and showering at these energies. It is impossible to attribute the structure entirely to any effects without carrying out simulations of possible backgrounds. The most likely source of events in the MC simulations are crossing events, from the 20 MeV γ emitted in the scintillator interacting within the scintillator via Compton scattering and pair production. It is expected that the MC plots would look significantly different if time of flight cuts to exclude crossing events were used.

The required parameters for the halflife limit from Equation 21 can now be obtained from the data and MC information. The data sample gives N_{decay} (the number of PEP violating decays found in the data sample, assuming all of the events are attributed to PEP violating transitions) and the length of the measurement (834.002 days). The efficiency, η, is obtained from the petal and wall MC separately. The initial number of atoms in the sample, N_0, is obtained from the total scintillator mass in NEMO. There is 5400 kg of scintillator in the walls and 1000 kg of scintillator in the petals, making a total of 6400 kg of scintillator.

From the distribution of the data it can be seen that most of the structured events are below ~ 8.5 MeV (except the saturation peak at higher energies), above which the background becomes flat. Therefore to obtain the number of PEP violating decays from the data and the efficiency of event detection from the MC a cut at 8.5 MeV is made. 104 events were found in the data above 8.5 MeV, 32467 events in the wall MC and 2611 events in the petal MC (for ten million simulated events).

To obtain a 90% CL limit for PEP violation 1.28σ (for a distribution not centred around zero) must be added to the number of PEP violating events found in the data above 8.5 MeV. Photon statistics obey Poissonian statistics:

$$\sigma = \sqrt{N} \tag{15}$$

Therefore, for 104 at 90% CL the number of PEP violating events in data becomes 117.05. Efficiency is calculated as number of events detected divided by number of events simulated (ten million). Therefore, the efficiency for the wall MC is $3.2467 \times 10^{-3} = 0.325\%$ and for the petal MC is $2.611 \times 10^{-4} = 0.026\%$.

To calculate the number of molecules in the wall and petal scintillators the atomic mass of one molecule of scintillator must be found. The composition of the scintillator is C_8H_8, therefore the atomic mass of one molecule is:

$$(8 \times 12.01 \text{ gmol}^{-1}) + (8 \times 1.01 \text{ gmol}^{-1}) = 104.1 \text{ gmol}^{-1} \tag{16}$$

The number of molecules in the scintillator is determined by:

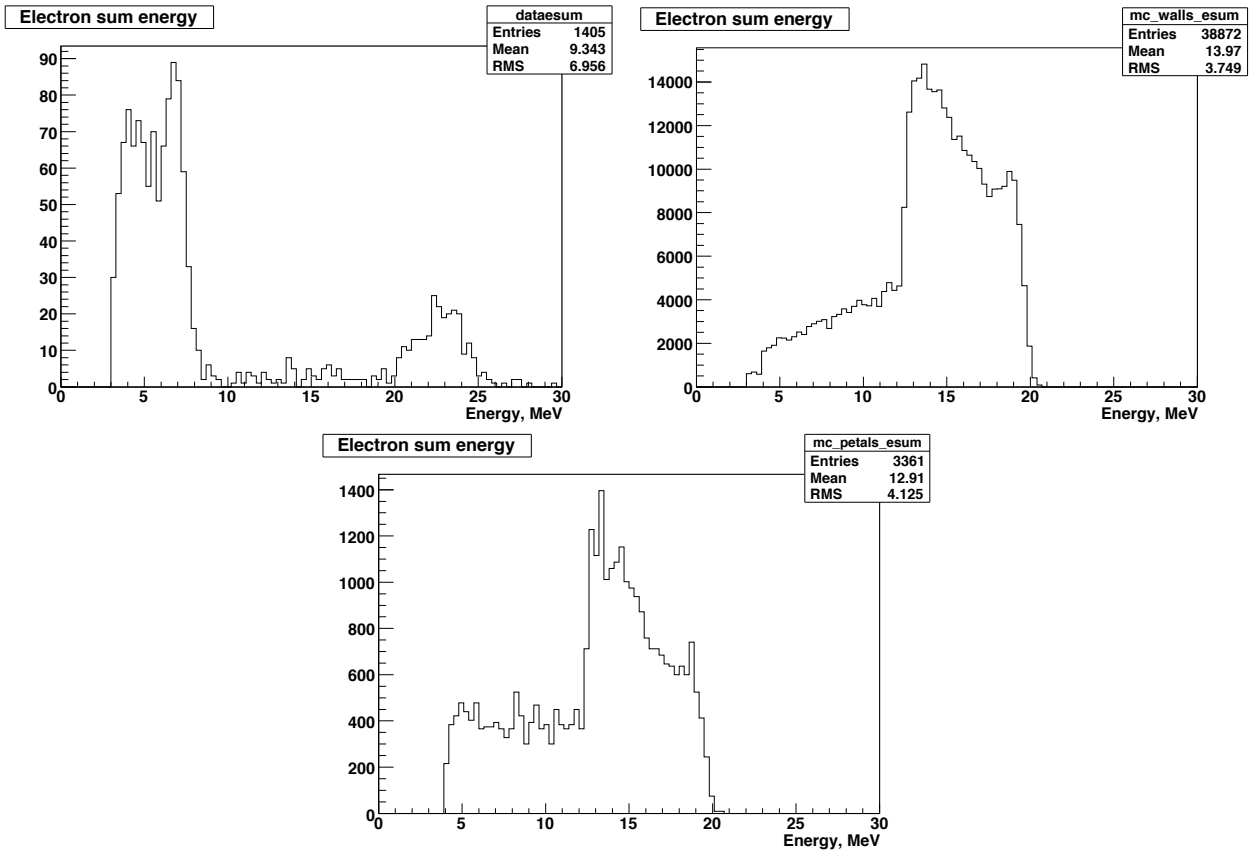

Figure 6: $\gamma \longrightarrow e^+e^-$ events in data, wall MC simulations and petal MC simulations

$$\text{number of molecules in scintillator} = \frac{\text{mass of scintillator}}{\text{mass of 1 molecule of scintillator}} \tag{17}$$

Each molecule contains 8 molecules of carbon and as ^{12}C is 98.98% abundant the number of ^{12}C in the scintillator is:

$$\text{number of molecules of } ^{12}C = \text{number of molecules of scintillator} \times 8 \tag{18}$$

Therefore the number of ^{12}C atoms in the scintillator is:

$$N_0 = \text{number of molecules of } ^{12}C \times N_A \tag{19}$$

The number of ^{12}C atoms in the NEMO3 scintillators, N_0, is 2.96×10^{29}. To calculate the limit the efficiencies must be added with appropriate weights, relative to the masses of the wall and petal scintillators:

$$\eta = (x_{walls}\eta_{walls} + ((1 - x_{walls})\eta_{petals}) \tag{20}$$

where x_{walls} is the fraction of mass in the wall scintillators ($= \frac{5.4}{6.4}$), η_{walls} is the efficiency of the wall scintillators and η_{petals} is the efficiency of the petal scintillators. The combined efficiency from wall and petal scintillator efficiencies is $2.780 \times 10^{-3} = 0.278\%$. Substituting all of the obtained parameters into Equation 21 the halflife limit obtained is:

$$T_{1/2} > 1.1 \times 10^{25} \text{ years} \tag{21}$$

Considering all of the possible eight transitions for $\gamma \longrightarrow e^+e^-$ in Figure 4a the limit on the PEP violating transitions of a nucleus from the p shell to the fully occupied s shell in ^{12}C at 90% CL is:

$$T_{1/2} > 8.9 \times 10^{25} \text{ years} \tag{22}$$

The NEMO2 experiment, a prototype of NEMO3, published a PEP violating limit for the $\gamma \longrightarrow e^+e^-$

transition in ^{12}C of $T_{1/2} > 4.2 \times 10^{24}$ years at 90% CL [7]. The result shown in Equation 22 is an order of magnitude higher. The Borexino Counting Test Facility (CTF), a prototype of the Borexino solar neutrino experiment, has also obtained a limit on the same transition of ^{12}C to non-Paulian states of $T_{1/2} > 2.1 \times 10^{27}$ years [8], a result one order of magnitude higher than the result presented here. Although CTF has a higher efficiency (4.3×10^{-2}) and less background than NEMO3, NEMO3 has more scintillator mass (a total of 6.4 tonnes compared to 4.2 for CTF), therefore there is a chance of obtaining a better limit if the background and the efficiency can be improved. This requires further study of event selection criteria, particularly understanding the high energy corrections for the time of flight information.

4.3 Future Plans for PEP Analysis

There is a lot of room for improvement to be made in the $\gamma \longrightarrow e^+e^-$ PEP violating channel. A high energy correction must be applied to the time of flight information, which can then be used in the cuts. The limit can be improved by increasing the efficiency of event selection without introducing too much background. A lot of events are lost by applying the two electron track requirement. In a lot of cases the PEP violating transition will not produce two electron tracks. For example, if the 20 MeV γ interacts within the scintillator, where it is produced, and undergoes Compton scattering knocking an electron in the scintillator out of orbit then only one track will be seen. It could be more efficient to search for high energy deposits in the scintillators.

Once the best limit for this channel is obtained the β decay channel must also be analysed. If the limits obtained will be the world's best then a publication is possible. In order to achieve this the analysis must be completed as soon as possible before Borexino can publish the results of the actual experiment rather than the prototype.

5 SuperNEMO Research and Design

The SuperNEMO experiment is the next step up from NEMO3 and is currently in its R&D phase. SuperNEMO will be based on the same principles as NEMO3 but will have an order of magnitude more isotope mass - 100 kg of either ^{82}Se or ^{150}Nd (if its enrichment is possible). The aim of the experiment is to achieve a sensitivity of $> 10^{26}$ years corresponding to an effective mass of $0.04 - 0.11$ eV. In order to achieve this it is extremely important to have the best possible energy resolution. The desired resolution for SuperNEMO is $\sim 7\%$ at 1 MeV, which requires using PMTs with a very high quantum efficiency (QE) of at least 35%. A lot of research into combinations of setups for the calorimeter that will give the best resolution is being carried out.

The main approach for SuperNEMO is to have a baseline design consisting of 20 modules, each of which will contain 5 kg of source. The advantages of this design are that each module will be a fully operational detector on its own therefore data taking can begin as soon as each module is completed and that there is a possibility to place the modules in separate underground laboratories if one that is large enough cannot be found to accommodate the entire detector. However, there is another possibility to consider - using scintillator bars.

5.1 Calorimeter Design Using Scintillator Bars

Instead of using the modular baseline design, which would involve using $\sim 12,000$ scintillator blocks and PMTs, it is possible to use scintillator bars (of 2 m length, ~ 10 cm width and ~ 2.5 cm thickness) for the calorimeter. This design would have the scintillator bars, placed vertically and stacked up next to each other horizontally, surrounding the source foils. The bars will be read out by a PMT at each end of the scintillator bar, as can be seen in Figure 7. This setup could then be arranged in rows and columns with a scintillator bar followed by a source foil followed by a scintillator bar etc. creating one large detector.

There are many advantages to this kind of design. It is much more compact than the baseline design - an 11×12 m^2 floor area will accommodate the required 100 kg of isotope (40 mgcm^{-2}) therefore eliminating the problem of finding a laboratory large enough to contain the experiment. The number of PMTs needed is drastically reduced from ~ 12000 for the baseline design to ~ 2900 PMTs. The baseline design will use 8 inch hemispherical PMTs (in order to withstand the vacuum and to have better timing resolution), which are more difficult and expensive to produce. However, the bars can be read out with 3 or 5 inch high QE flat PMTs. This will greatly reduce the cost of the experiment and will create a more radiopure atmosphere as fewer PMTs will be used. Another advantage of having fewer PMTs is that it will be easier to calibrate them. The external walls of the detector can act as passive shielding by using anti-coincidences leading to

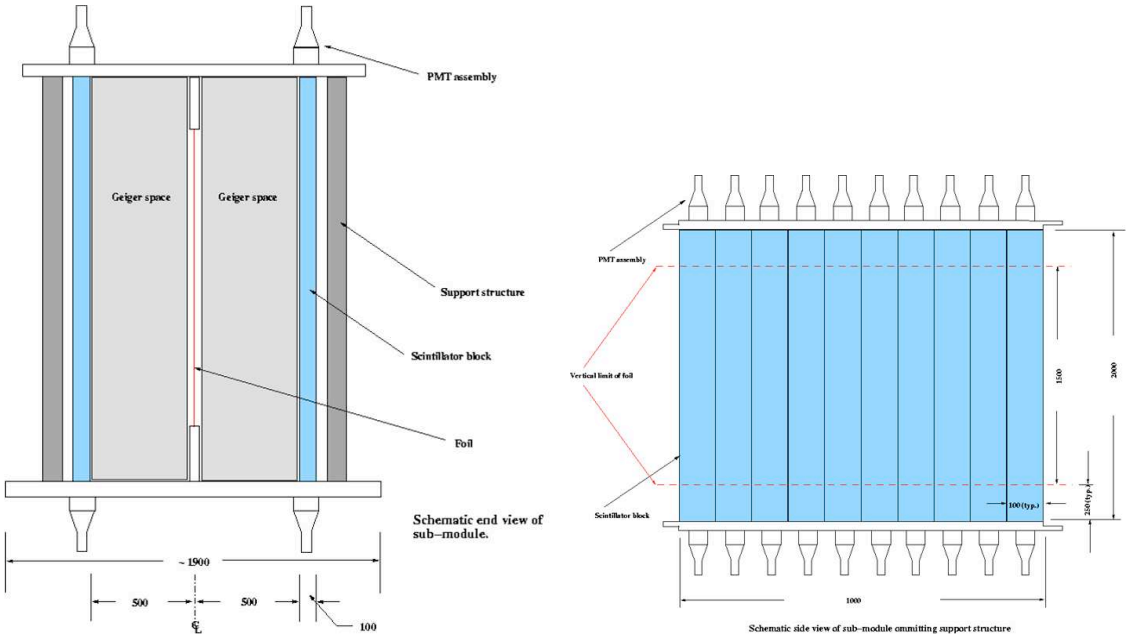

Figure 7: SuperNEMO using scintillator bar design: cross sectional and side views

better background suppression, meaning that the time of flight requirements could possibly be relaxed. This would allow a smaller distance between the scintillator and the source foil, which has been shown to increase efficiency in simulations. The bars also provide increased impact resolution of $1-2$ cm. For these reasons it is a possibility that an energy resolution of $\sim 10-11\%$ at 1 MeV could be enough to achieve the desired sensitivity. However, simulations need to be carried out to confirm this.

A design implementing scintillator bars has many advantages. The main challenge presented is reaching a high enough energy resolution - one that will enable SuperNEMO to reach its planned sensitivity. A lot of R&D work must be done in order to see whether the scintillator bar design is a feasible one.

5.1.1 Scintillator Bar Testing

The scintillator bar that the tests were carried out on has dimensions of 2 m $\times 10$ cm $\times 1.25$ cm and is a BC408 plastic scintillator, which has a long optical bulk attenuation length (380 cm) and fast timing, making it a good scintillator to use for time of flight systems [9]. The scintillator bar is read out by a PMT at each end, with a possibility of two different PMTs. The first is a 3 inch Super Bialkili (SBA)-select Hamamatsu tube (essentially a prototype of the Ultra Bialkili tube) with a QE of a maximum of $\sim 43\%$ at a wavelength of 350 nm [10], made available for SuperNEMO testing before it is generally available on the market. The second is a 5 icnh ETL 9390 tube with a QE of $\sim 28\%$. When using the 3 inch PMT the width of the scintillator is greater than the diameter of the PMT, therefore two plastic lightguides were designed to direct the collected light from the ends of the scintillator bar to the PMTs. The lightguides were polished by hand and coupled to the scintillator and PMT joints with optical grease in order to achieve the highest possible light collection. Another way to increase light collection is to wrap the scintillator bar in either mylar or Enhanced Specular Reflector (ESR, reflection coefficient of $\sim 98\%$). The setup is then placed within a black box covered by a black cloth in order to exclude any outside light.

The data acquisition (DAQ) system works in the following way. The two PMT signals are read out and sent to a 50 Ω splitter (which was soldered especially for the DAQ), dividing the signal into two. One of the split signals then goes to the ADC, whilst the other goes to a discriminator, creating a pulse which is used to trigger the gated TDC. The ADC and TDC data is collected simultaneously.

Four setups were tested in all, summarised in Table 1. The testing procedure is carried out in the following way. A ^{207}Bi source, which emits conversion electrons and γs, is scanned across nine different points (-80 cm, -60 cm, -40 cm, -20 cm, 0 cm, 20 cm, 40 cm, 60 cm and 80 cm, with 0 cm being at the centre of the bar) on the scintillator bar. It should be noted that an aluminium box is placed around the source to filter any electrons being emitted into the northern hemisphere, which can make false energy deposits in the scintillator. However, for the first setup (3 inch PMTs with lightguides, with the scintillator bar wrapped in mylar) this was not done. Four runs are carried out for each point. The first run is a

PMTs Used:	Lightguides?	Wrapped In:	Voltage: (V)
3 inch SBA-Select (Hamamatsu)	Yes	Mylar	1450
3 inch SBA-Select (Hamamatsu)	No	Mylar	1450
3 inch SBA-Select (Hamamatsu)	No	ESR	1450
5 inch 9390 (ETL)	No	ESR	1300 – 1400

Table 1: Scintillator bar test setups

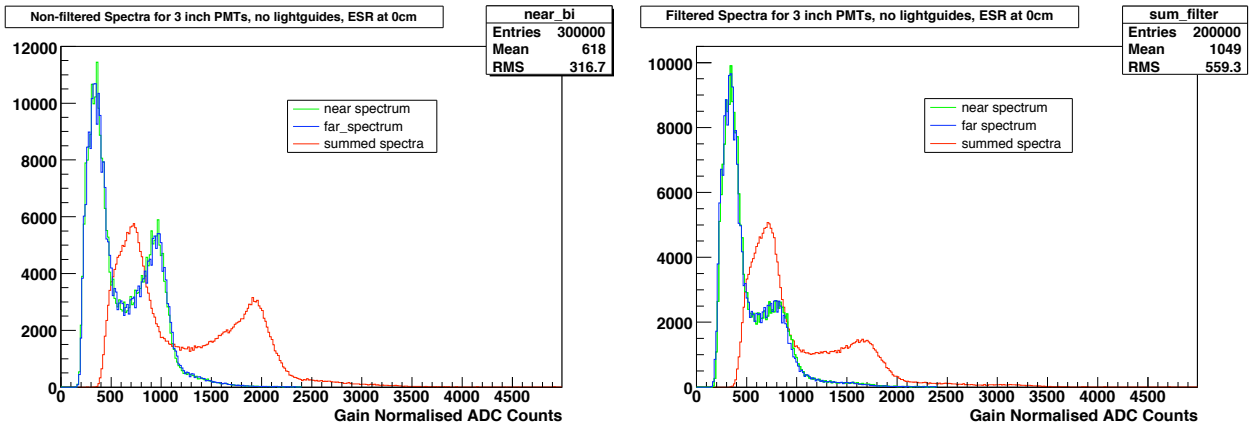

Figure 8: Acquired non-filtered and filtered scintillator bar spectra for the setup using 3 inch PMTs, without lightguides, wrapped in ESR at the 0 cm (i.e. central) position

pedestal run to measure any noise in the system, which can then be taken into account. The second run is taken with the ^{207}Bi source, where the energy from the electrons and the γs is converted into light by the scintillator and directed to the PMTs. The third run is again a pedestal run to ensure the electronics offset going to the ADC remains the same. The fourth run is taken with a 2 mm thick aluminium disk placed between the source and the scintillator, which filters the conversion electrons, producing a spectrum of the γs of the ^{207}Bi. The full and γ spectra are required for the energy resolution calculation. An example of the obtained spectra can be seen in Figure 8, which shows the individual and summed PMT spectra with and without the filter.

5.1.2 Scintillator Bar Analysis Procedure

To increase the light collected and improve the energy resolution the data acquired from each PMT at the ends of the bar is added. As it is possible that the PMTs used have slightly different gains, it is important to gain normalise the data before adding the spectra. This is done individually for the near and far PMT spectra. The non-filtered and filtered spectra are normalised to each other and the filtered spectrum is subtracted from the full spectrum to obtain the ^{207}Bi conversion electron spectrum alone. Figure 9 shows the normalised full and filtered spectra together and the conversion electron spectrum after the subtraction. There is a surplus of events in the filtered spectrum at low energies, which shows as a negative peak in the subtracted spectrum. This surplus is also seen in simulations. A possible explanation for this is due to a 570 keV γ always accompanying a conversion electron in the ^{207}Bi decay (see Section 5.1.4). As the scintillator bar is only half an inch thick and has a low atomic number there is a large possibility that the γ will not interact as there is not enough material. When an aluminium filter disk is introduced the γ from the source interacts with the aluminium, most likely by Compton scattering, producing a low energy electron which then interacts in the scintillator. The aluminium filter acts as a γ to electron converter, therefore creating a surplus of events when the filter is used.

Once the subtracted spectra are obtained the calibration constant for the near and far ends of the bar is then obtained by taking the difference between the two peak positions, which are expected to be at 976 keV and 482 keV, and dividing them by the energy difference between the two peaks (Equation 23). The ADC spectra obtained are then multiplied by the calibration constant event by event, after which the spectra can be added correctly and are ready for analysis. The spectra shown in Figure 8 have been gain normalised.

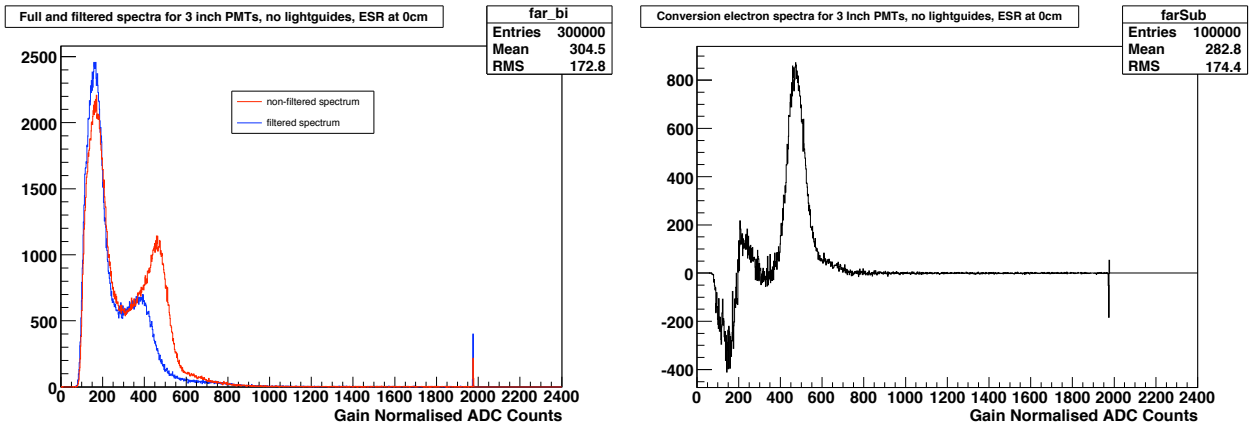

Figure 9: An example of normalised full and filtered spectra (left) and a subtracted spectrum (right) used to obtain the gain normalisation constant for the setup using 3 inch PMTs, without lightguides, wrapped in ESR at the 0 cm position

$$\text{calibration constant} = \frac{\text{976 keV peak position in ADC counts} \; - \; \text{482 keV peak position in ADC counts}}{494} \tag{23}$$

The energy resolution can be calculated from the spectra by obtaining the mean of the 976 keV conversion electron peak and the σ of the peak at FWHM:

$$\frac{\Delta E}{E} = \frac{\sigma_{FWHM}}{\mu} \tag{24}$$

where $\frac{\Delta E}{E}$ is the energy resolution, μ is the mean of the 976 keV conversion electron peak and $\sigma_{FWHM} = \sigma \times 2.35$. These values can be obtained by fitting the spectra. The fit works in the following way. At first the two γ lines of ^{207}Bi at 1.06 MeV and 0.57 MeV in the filtered spectrum are fitted with a Compton edge described by a variation of the Heaviside step function (Equation 25). The parameters obtained from this fit are then normalised and added to the fit for the entire spectrum, which is a combination of two triple Gaussian fits (for the k, l and m shells of the conversion electrons) at the 976 keV and 482 keV conversion electron peaks and the gamma lines [11]. The fit then returns the required parameters - the mean and σ of the k shell peak at 976 keV. The function of the fit for the 976 keV peak can be seen in Equation 26. An example of the fit can be seen in Figure 10 obtained from the 3 inch PMTs, no lightguides with the bar wrapped in ESR setup at the 0cm position. The parameters obtained from the fit are $\mu = 2165.78$ and $\sigma = 121.12$ giving a resolution of 12.93% at 1 MeV.

$$N \frac{e^{-C_1 x}}{1 + e^{(C_2 - x)/C_3}} \tag{25}$$

where N is the normalisation constant obtained from the fit and C_1, C_2 and C_3 are free constants for each gamma edge obtained from the fit.

$$N(7.03 \cdot G(\mu_K, \sigma_K) + 1.84 \cdot G(\mu_K + 72.1\alpha, \sigma_K \sqrt{1 + \frac{72.1\alpha}{\mu_K}}) + 0.545 \cdot G(\mu_K + 84.1\alpha, \sigma_K \sqrt{1 + \frac{84.1\alpha}{\mu_K}})) \tag{26}$$

where N is the refitted normalisation constant for the electron spectrum, G(μ, σ) is a Gaussian distribution with the mean μ and width σ and α is the calibration constant to convert the distance between the 976 and 482 keV peaks from keV into ADC units.

5.1.3 Results

According to MC, the best resolution should be achieved at the ends of the bar, where one of the PMTs is getting most light, whilst the worst resolution should be in the central position (although this should not

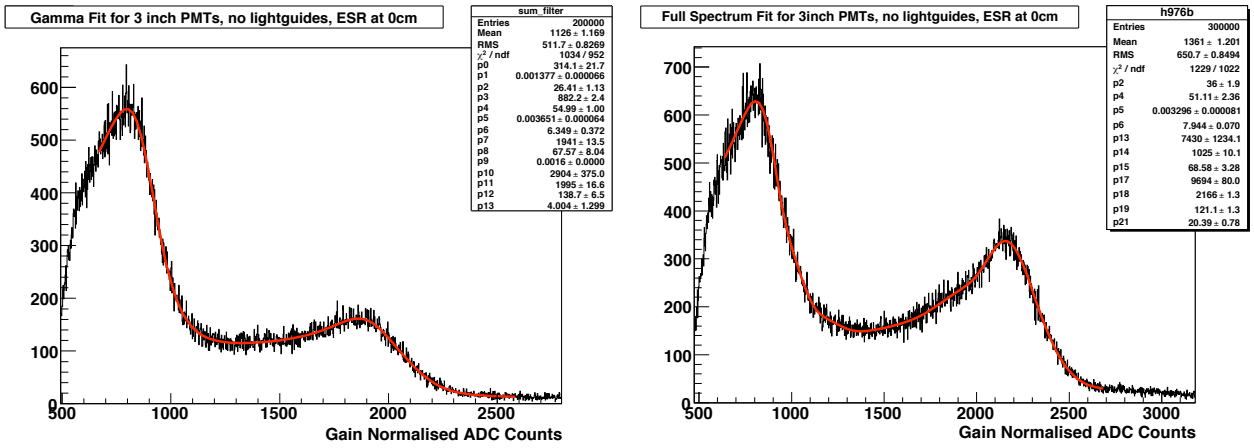

Figure 10: An example of the fitting procedure for the setup using 3 inch PMTs, without lightguides, wrapped in ESR at the 0 cm position, giving a resolution of 12.93%

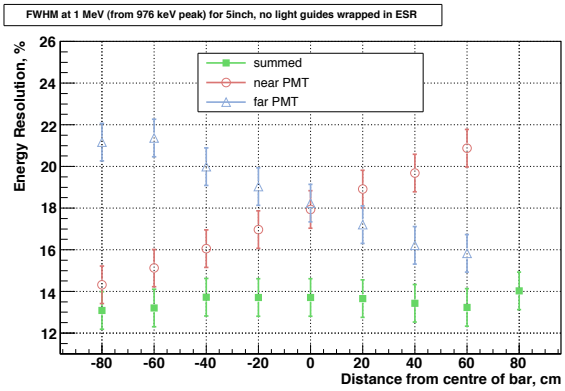

Figure 11: Resolution for the 5 inch PMTs, no lightguides, ESR setup

vary by more than $\sim 1\%$). When analysing the individual PMT spectra (rather than the sum) the resolution should be highest at the end where the source is placed and lowest at the end farthest away from the source. Seeing this trend in the individual PMT results would show that the fit is working correctly. The resolutions obtained for the 5 inch PMTs, no lightguides, wrapped in ESR setup can be seen in Figure 11. The trend expected from the individual PMTs can be seen, with the resolutions being very similar at 0 cm ($\sim 18\%$ FWHM at 1 MeV), excluding one point in the far PMT analysis at -80 cm. The pattern for the summed PMT resolutions is also as expected, with the exception of the point at 80 cm. For both the individual and the summed PMTs the spectra at the far ends of the bar appear very squashed together, making it more difficult to obtain a good fit. The errors shown on the plot are systematic errors obtained from the fit to the generated MC.

The energy resolution obtained from the sum of the PMTs for all of the setups tested can be seen in Figure 12 (where the error bars are shown for only some of the setups in order to make the plots clearer). The results vary between 12% and 14.3%. The setup giving the best resolutions is one that uses 3 inch PMTs without lightguides wrapped in mylar. Although some of the light is being lost between the bar and the PMT (due to the bar width being larger than the PMT diameter) it seems that this setup provides better results than when using lightguides. It should be noted that the setup with the lightguides was tested without the aluminium box around the source shielding the bar from electrons emitted into the northern hemisphere. It is expected that the box provides an improvement of $\sim 1\%$, however this could not be confirmed as not enough time was available to repeat the measurements. It is very difficult to get a good connection between the bar and the lightguide as the setup is difficult to access and the two areas being connected are so small, therefore light is being lost.

It is also unexpected that a mylar and an ESR setup give very similar results as due to ESR's higher reflectivity coefficient light collection should be improved for the ESR setup. In order to investigate this the light outputs of the mylar and ESR in identical setups (3 inch PMTs without lightguides) were looked at.

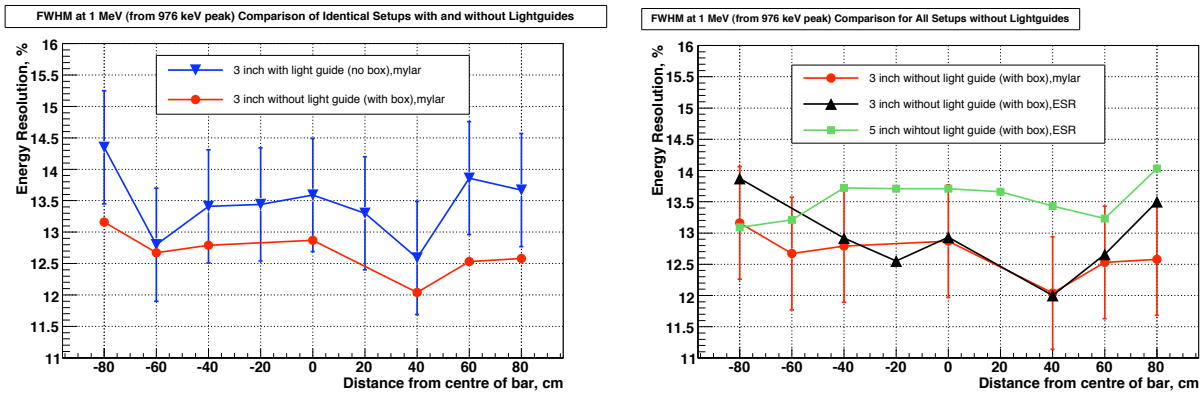

Figure 12: Scintillator bar resolutions for all of the tested setups: setups using lightguides are shown on the left and setups without lightguides on the right. The errors are only shown for one setup on each plot in order to make the plots more legible.

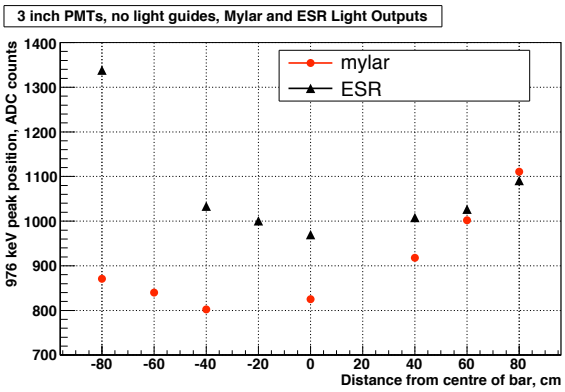

Figure 13: Mylar vs. ESR: light outputs for the 976 keV peak in ADC counts for identical setup conditions

Figure 13 shows the 976 keV peak position in ADC counts for the mylar and ESR setups. The light output of the mylar seems to increase at the far end of the bar, whilst the ESR light output decreases at that end. A possible explanation for this is that at the far end of the bar the mylar wrapping was less tight than at the near end, creating an air gap between the mylar and the scintillator bar. Simulations show that an air gap increases the light collection [12], which could be the effect seen here. However, for the ESR case the far end of the setup was very dirty with optical grease (due to limited time available to create the setup), attracting dust and other dirt, which could worsen light collection. At certain points, particularly at -80 cm, the light output of the ESR is $\sim 50\%$ higher than that of the mylar, so clearly there is an increase in light output, which we expect to see translated into the resolution. However, the resolution does not at all improve for the ESR setup. Simulations show that the bar scintillator setup should achieve an energy resolution of $\sim 9-10\%$ [12], however we are not seeing results as good as this. Could there be a factor that is limiting the resolution?

5.1.4 Pile Up - the Limiting Factor

When considering the ^{207}Bi decay chain, the ^{207}Bi captures one of its shell electrons and becomes ^{207}Pb. This leaves the lead in an excited state. In order to get back to the ground state it de-excites via two γ emissions. There is a chance that instead of a γ emission this process can happen via an electron conversion at 976 keV, which will almost always be accompanied by a ~ 570 keV γ (unless this also happens via electron conversion, which has an incredibly small probability of occurring). As this happens simultaneously the bismuth spectrum gets broadened, therefore worsening the resolution. At the same time, when the bismuth captures an electron and becomes lead, the bismuth is left with a "hole" and the remaining electrons cascade down to lower orbits, emitting an X-ray of $\sim 15-30$ keV.

Therefore a "pile up" effect becomes apparent as the 976 keV conversion electron is always accompanied

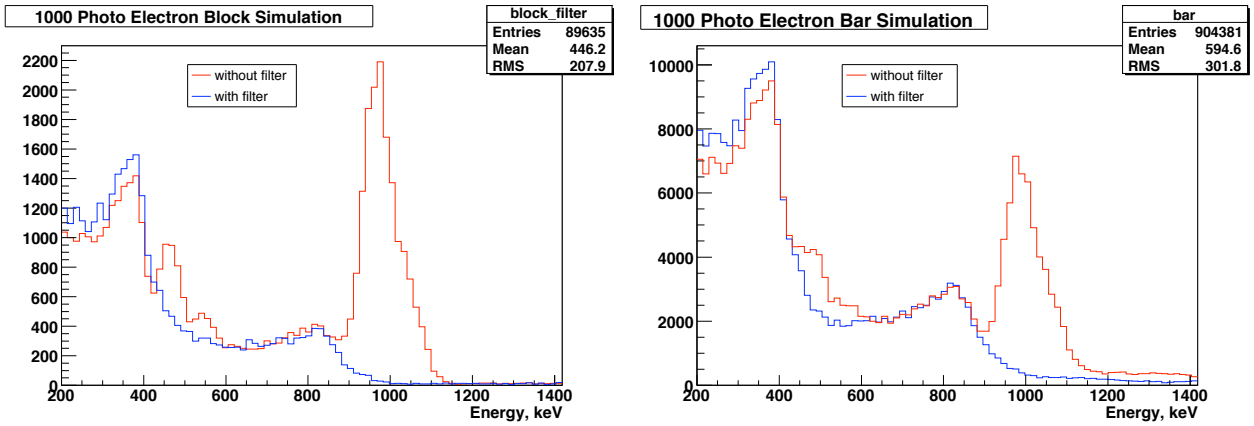

Figure 14: Pile up simulations for a 1000 photo electron output for the block geometry (left) and the bar geometry (right)

by a 570 keV γ and a $15-30$ keV X-ray. Due to the solid angle in the geometry of the bar testing these γs and X-rays are more likely to be picked up by the scintillator therefore worsening the resolution. In order to see how big an effect this is simulations must be run to take the pile up into consideration.

5.1.5 Pile Up Simulations

In order to see how much the pile up affects the scintillator bar geometry compared to scintillator block geometry (which is also being tested by UCL and other collaborators for the baseline modular design of SuperNEMO, for a block with dimensions of 5 cm $\times$5 cm $\times$2 cm with an air gap of 6 cm between the scintillator and the source) simulations using GEANT 3.21 for geometry descriptions and genBB for the ^{207}Bi decay description were carried out. The simulation is run for a specific energy resolution by reading in the number of photoelectrons that the PMT sees. The number of photo electrons is converted into energy resolution in the following way:

$$\delta = \frac{\sigma}{N} = \frac{\sqrt{N}}{N} = \frac{1}{\sqrt{N}} \tag{27}$$

where N is the number of photo electrons and σ is the error on the number of photo electrons, calculated from Poissonian statistics as $\sqrt{N}$. This can then be converted into energy resolution at FWHM by multiplying by 2.35. Therefore to obtain a simulated spectrum for an energy resolution of, for example, 7.34% FWHM at 1 MeV the simulation would be given 1000 photo electrons as an input.

The pile up effect is included in the physics description of the decay, therefore by calculating the energy resolution of simulated MC for the bar and block geometries it can be seen how each is affected. As the fit used on the data fits the filtered spectrum and then applies the obtained parameters to the full spectrum the aluminium disk must also be included in the simulation and the simulation must be run with and without the filter. The simulations were run for four different light outputs: 1000, 800, 600 and 400 photo electrons. Figure 14 shows the spectra obtained for the block (four million events simulated) and the bar (two million events simulated) setups with and without the filter for a 1000 photo electron output. It can immediately be seen that the peak in the bar simulation is wider (more smeared) than in the block simulation showing that the pile up affects the bar setup more severely, as expected. The resolution is 7.63% FWHM at 1 MeV (0.29% away from MC truth of 7.34% FWHM at 1 MeV for a 10000 photo electron output) for the block setup and 7.88% FWHM at 1 MeV (0.54% away from MC truth) for the bar setup. The resolution for the bar setup is roughly twice the value the block resolution is away from MC truth.

The results obtained for all of the light outputs simulated can be seen in Table 2. For photo electron outputs of 1000, 800 and 600 the block setup resolution remains a $\sim$ constant 0.27% away from MC truth, whilst the bar setup resolution is a $\sim$ constant 0.55% away from MC truth - twice worse than the block setup. This shows that the pile up effect has a larger impact on the scintillator bar setup. For the 400 photo electron output the resolutions decrease more than expected for both the block and bar setups.

There are a number of solutions to attempt to fix the pile up problem for the bar setup. The source could be lifted up from the bar creating an air gap between the source and the bar so that the γ has more of

Light Output: (Photo electrons)	Monte Carlo Truth: (FWHM at 1 MeV)	Block Setup Resolution: (FWHM at 1 MeV)	Bar Setup Resolution: (FWHM at 1 MeV)
1000	7.34%	7.63%	7.88%
800	8.21%	8.47%	8.74%
600	9.47%	9.73%	10.05%
400	11.61%	12.34%	12.48%

Table 2: Energy resolution for block and bar setups for various light outputs

a chance of interacting in the air. However, this is unlikely to make much of a difference. Some sort of lead shielding to stop the γs could be considered, however this would be heavy, bulky and difficult to implement into the bar setup as there is limited space inside the box the setup is contained within. The most logical solution is to run simulations for the bar setup at energy resolutions of 0.1% intervals to produce all possible resolutions that can be obtained with the bar tests. The data spectra can the be fitted to the MC spectra with the best fit giving the energy resolution. This can also be implemented for the block setup as, though to a smaller degree, pile up also affects that setup. This will provide an all round more accurate method of obtaining the energy resolution from the measured spectra.

Whilst pile up affects SuperNEMO R&D it will not affect the actual experiment as SuperNEMO will not use a ^{207}Bi source therefore will not have the problem of disentangling the 570 keV γ from the conversion electron.

5.2 Future Plans for Scintillator Bar Tests

The TDC data obtained with the setups already tested must be analysed.

The bar tests carried out so far need to be repeated with a more accurate setting up procedure (now that there are slightly less time constraints) to ensure that the setup is uniform (for example if there is an air gap between the reflector wrapper and the scintillator then it must be uniform throughout). This could be done by introducing some sort of tube to go around the scintillator bar that the mylar or ESR could be placed in.

There are many more possibilities for setups. For example, the ends of the bar could be tapered to fit the diameter of the high QE 3 inch PMTs so that light is not lost at the parts not covered by the PMTs. A number of scintillator bars (equivalent to BC408) from a different manufacturer, ELJEN, have been ordered: one with very similar dimensions to the current bar except a thickness of one inch and ends tapered to fit the 3 inch PMTs and several with an altered width of 6.5 cm so that the bar would fit entirely within the 3 inch PMT.

Most importantly, the simulations for different resolutions of bar and block setups must be carried out (with very high statistics) in order to have a correct fitting procedure.

6 Conclusions

Since beginning work on NEMO3 and SuperNEMO I have done a lot of interesting and stimulating work in areas of analysis, R&D and simulations. I have started on, and will continue, to analyse NEMO3 data to obtain a limit on PEP violating transitions in the ^{12}C of the scintillators. I am aiming to publish this result if I can obtain the world's best limit. Once the PEP violation analysis is complete I plan to extend the $\gamma \longrightarrow e^+e^-$ analysis to study the number of these events occurring in NEMO3 from all possible sources. I will then extrapolate this result to see how many of these background events, which can mimic double beta decay, can be expected in SuperNEMO to study whether the experiment will need a magnetic field to suppress them.

I have contributed to the tracker (although not mentioned here) and calorimeter development of SuperNEMO already and will make a lot of further progress on this. I have already been to and presented my findings at three NEMO collaboration meetings. It has been incredible to work on such a variety of things and I am very grateful to everyone who has made that possible.

References

[1] David Griffiths, *Introduction to Elementary Particles*, Wiley-VCH, 2004

[2] S. M. Bilenky, physics/0603039, 2006

[3] Boris Kayser, *Neutrino Physics*, Fermilab, Batavia IL 60510, USA arXiv:hep-ph/0506165 v1, 2005

[4] Karsten M. Heeger, *Evidence for Neutrino Mass:A Decade of Discovery*, Lawrence Berkley National Laboratory (University of California), LBNL-56717, 2004

[5] W. H. Furry, *On Transition Probabilities in Double Beta Disintegration*, Phys. Rev. 56, 1184-1193, 1939

[6] H. V. Klapdor-Kleingrothaus et al., *Latest Result from the Heidelberg-Moscow Experiment*, Eur. Phys. J. A. 12, 147-154, 2001

[7] A. S. Barabash for the NEMO Collaboration,*Testing the Pauli Exclusion Principle with the NEMO2 Detector*, Nuclear Physics B (Proc. Suppl.) 87 (2000) 510-511

[8] A. Derbin for the Borexino Collaboration, *Physics Outside the Standard Model with the Prototype of the Borexino Detector*, Nuclear Physics B (Proc. Suppl.) 143 (2005) 568

[9] Bicron BC408 Polyvinyltoluene Plastic Scintillator Data Sheet, http://www.detectors.saint-gobain.com/Data/Element/Node/Category/category_edit.asp?ele_ch_id=C0000000000000001855

[10] Hamamatsu website, http://jp.hamamatsu.com/resources/products/etd/eng/html/pmt_003.html

[11] Matthew Kauer, University College London, private communications, 2008

[12] Benton Pahlka, University of Texas, private communications, 2008